

# Statistical distributions of singular vectors for tropical cyclones affecting Korea over a 10-year period

Sei-Young Park · Hyun Mee Kim · Tae-Young Lee ·  
Michael C. Morgan

Received: 16 July 2012 / Accepted: 7 March 2013 / Published online: 28 March 2013  
© The Author(s) 2013. This article is published with open access at Springerlink.com

**Abstract** To investigate the statistical sensitivity distributions of tropical cyclone (TC) forecasts over the Korean Peninsula, total energy (TE) singular vectors (SVs) were calculated and evaluated over a 10-year period. TESVs were calculated using the fifth-generation Pennsylvania State University/National Center for Atmospheric Research Mesoscale Model (MM5) and its tangent linear and adjoint models with a Lanczos algorithm over a 48-h period. Chosen cases were 21 TCs that affected the Korean Peninsula among 230 TCs that were generated in the western North Pacific from 2001 to 2010. Sensitive regions indicated by TESVs were mainly located near mid-latitude troughs and TC centers but varied depending on TC track and environmental conditions such as subtropical high and mid-latitude trough. The cases were classified into three groups by clustering TC tracks based on the finite mixture model. The two groups that passed through the western and southern sea of the Korean Peninsula had maximally sensitive regions in the mid-latitude trough and largely sensitive regions around the TC center, while the other group that passed straight through the eastern sea of the Korean Peninsula had maximally sensitive regions near the north-eastern region of the TC center. Vertically, the former two clustered groups had the westerly tilted TESVs and

potential vorticity structures under the mid-latitude troughs at the initial time, indicating the TCs were in a baroclinic environment. Conversely, the straight-moving TCs were not in a baroclinic environment. Based on the results in the present study, the TCs moving toward a fixed verification region over the Korean Peninsula have different sensitivity regions and structures according to their moving tracks and characteristic environmental conditions, which may provide guidance for targeted observations of TCs affecting the Korean Peninsula.

## 1 Introduction

Considerable effort has been made to increase the accuracy of tropical cyclone (TC) forecasts by studying TC dynamics and structures (Kurihara and Tuleya 1974; Frank 1977a, b; Wang 2002; Kwon and Frank 2005, 2008) and by investigating the relationship between TCs and the environment using observational or reanalysis data from numerical weather prediction (NWP) models (Holland and Wang 1995; Ho et al. 2004; Byun and Lee 2012), as well as by developing an NWP model for TCs (Rappaport et al. 2009; Dorst 2007).

When considering the accuracy of the NWP model, there are two types of error: the model error and the initial condition uncertainties. Adaptive (or targeted) observations have been applied to TCs to increase the accuracy of TC forecasts by decreasing the initial condition uncertainties (Peng and Reynolds 2005, 2006; Kim and Jung 2006, 2009a, b; Kim et al. 2011a; Jung et al. 2012; Majumdar et al. 2006; Wu et al. 2007, 2009a, b; Lang et al. 2012). The observational regions detected by adaptive observation strategies are called sensitive regions because the observations in those regions may have a large influence on enhancing weather forecasts (Kim et al. 2004a). Singular

Responsible editor: M. Kaplan.

S.-Y. Park · H. M. Kim (✉) · T.-Y. Lee  
Department of Atmospheric Sciences, Yonsei University,  
50 Yonsei-ro, Seodaemun-gu, Seoul 120-749,  
Republic of Korea  
e-mail: khm@yonsei.ac.kr

M. C. Morgan  
Department of Atmospheric and Oceanic Sciences,  
University of Wisconsin–Madison, Madison, USA

vectors (SVs) have been used to detect regions of high sensitivity to small perturbations for the purpose of making adaptive observations (Palmer et al. 1998; Buizza and Montani 1999; Gelaro et al. 1999; Montani et al. 1999; Peng and Reynolds 2005, 2006; Kim and Jung 2009a, b) because they are the fastest growing perturbations during a specified time period (i.e., the optimization interval) for a given norm and basic state (Kim and Morgan 2002).

There have been two kinds of studies applying SVs for TC forecasts. One is a case study and the other is a statistical or composite analysis applied to many cases. As a case study, Kim and Jung (2009a) evaluated the SV sensitivities near a TC center and at midlatitude and interpreted the dynamical interactions between the recurving TC and the mid-latitude system. In addition, Kim and Jung (2009b) investigated the effects of moist physics and norm on SV structures of Typhoon Usagi (0705). As a composite analysis, Peng and Reynolds (2006) studied 85 TC cases that were generated in the western North Pacific from July to October 2003 and divided them into two groups (straight- and non-straight moving TCs) to determine the SV characteristics due to TC movements. Reynolds et al. (2009) chose 84 cases from the 18 TCs generated in 2006 to investigate SV sensitivities and downstream impacts. Chen et al. (2009) studied the same cases as Reynolds et al. (2009) except for the extratropical transition (ET) cases and focused on the dynamic relationship between TC evolution and the surrounding synoptic-scale features.

Several observational and simulation studies have already shown that TC evolution and movements are closely associated with the surrounding environment (e.g., the subtropical ridge and extratropical trough). Wang et al. (1993) found that TC motion in a baroclinic environment can be sensitive to the diabatic heating and the vertical structures of both the vortex and its environment. Holland and Wang (1995) indicated that recurvature can occur through an unbroken subtropical ridge at the initial time, but that the mid-latitude trough considerably strengthens the potential for recurvature. Holland and Wang (1995) further suggested that vorticity and environmental changes in the middle and lower levels may be more significant for general environmental interactions leading to recurvature than those in the upper troposphere. Wu et al. (2009b) stated there are several dynamic systems affecting the TC motion in the western North Pacific, such as the subtropical high, the mid-latitude trough, the subtropical jet, and the southwesterly monsoon.

Previous sensitivity studies using SVs and adjoint sensitivities reaffirm the important relationship between TCs and surrounding environments on TC movements and evolution. Nevertheless, none of the previous studies focused on the TCs affecting the Korean Peninsula over an extended period. In addition, the previous statistical sensitivity analysis for TCs that occurred in the western North

Pacific focused on several TCs that occurred in specific years, which may not represent long-term sensitivity characteristics. Therefore, the present study investigated the statistical TESS distributions of the TC forecasts affecting the Korean Peninsula during the past 10 years. The distinct characteristics of the present study that differ from the previous studies are that only one case is chosen for each TC, the experimental period is long (10 years, from 2001 to 2010), and the verification region is fixed to the Korean Peninsula for all experiments.

Section 2 describes the methodology and experimental framework, while Sect. 3 describes the results, and Sect. 4 contains a summary and discussion.

## 2 Methodology and experimental framework

### 2.1 Singular vector calculation

As described in Kim and Jung (2009b), the calculation of SVs involves selecting an initial disturbance with the constraint that it has the unit amplitude and evolves to have maximum amplitude in a specified norm after some finite optimization time. In this study, the initial and final norms used were the dry total energy (TE) defined by Zou et al. (1997) as:

$$E_d = \iiint_{\sigma, y, x} \frac{1}{2} \left[ u'^2 + v'^2 + w'^2 + \left( \frac{g}{N\bar{\theta}} \right)^2 \theta'^2 + \left( \frac{1}{\bar{\rho}c_s} \right)^2 p'^2 \right] dx dy d\sigma, \quad (1)$$

where  $E_d$  is dry TE in a non-hydrostatic model;  $u'$ ,  $v'$  and  $w'$  are the zonal, meridional, and vertical wind perturbations, respectively;  $\theta'$  is the potential temperature perturbation;  $p'$  is the pressure perturbation;  $\bar{N}$ ,  $\bar{\theta}$ ,  $\bar{\rho}$ , and  $c_s$  are the Brunt–Väisälä frequency, potential temperature, density, and speed of sound at the reference level (500 hPa), respectively; and  $x$ ,  $y$ , and  $\sigma$  denote the zonal, meridional, and vertical coordinates, respectively.

The amplitude of the perturbation state vector ( $x'$ ) in the specific norm  $C$  was defined as:

$$\langle x'(t), Cx'(t) \rangle = \langle Mx'(0), CMx'(0) \rangle, \quad (2)$$

where the inner product is denoted by  $\langle \cdot, \cdot \rangle$ ,  $M$  is the tangent linear model (TLM) of the non-linear model, and  $C$  is the matrix operator appropriate to the specific norm.

In (2), the state vector at the initial time was assumed to evolve linearly. The constrained optimization problem seeks to maximize the amplification factor:

$$\lambda^2 = \frac{\langle PMx'(0), CPMx'(0) \rangle}{\langle x'(0), Cx'(0) \rangle} \quad (3)$$

at the optimization time, where  $\mathbf{P}$  is a local projection operator that makes the state vector zero outside a given domain (Buizza 1994). That domain was the verification region in the present study. A local projection operator was employed to optimize the final-time perturbation energy in a  $20^\circ \times 20^\circ$  box, as in Peng and Reynolds (2006), Reynolds et al. (2009), and Chen et al. (2009), centered on the final-time TC position ( $33.530^\circ\text{N}$ ,  $128.975^\circ\text{E}$ ) that was the median of the 48-h TC forecast centers and included the Korean Peninsula.

The maximum of the ratio in (3) is realized when  $\mathbf{x}'(0)$  is the leading SV of TLM  $\mathbf{M}$  for the  $\mathbf{C}$  norm, that is, when  $\mathbf{x}'(0)$  satisfies the following:

$$\mathbf{M}^T \mathbf{P}^T \mathbf{C} \mathbf{P} \mathbf{M} \mathbf{x}'(0) = \lambda^2 \mathbf{C} \mathbf{x}'(0). \quad (4)$$

The generalized eigenvalue problem in (4) can be reduced to an ordinary eigenvalue problem by multiplying both sides with the inverse of the square root of  $\mathbf{C}$ . Then a Lanczos-type algorithm (e.g., Ehrendorfer and Errico 1995) is used to solve for  $\mathbf{x}'(0)$ .

To investigate the overall properties of the first to third TESVs for each case, the vertically integrated energy composites from the first to third TESVs were calculated as:

$$s_{ij}^{\text{composite}} = \sum_{n=1}^3 \left( \frac{\lambda_n^2}{\lambda_1^2} \right) S_{ij}^n, \quad (5)$$

where  $i$  and  $j$  denote grid points in the  $x$  and  $y$  directions,  $\lambda_1^2$  and  $\lambda_n^2$  are singular values for the first and the  $n$ th TESVs, respectively, and  $S_{ij}^n$  denotes the  $n$ th vertically integrated TESV energy field as in Kim and Jung (2009b) and Kim et al. (2011a).

The normalized average TESV for all TC cases was obtained by averaging TESVs for individual cases that were normalized by the largest value, as in Reynolds et al. (2009).

## 2.2 Model and data

As in Kim and Jung (2009a, b) and Kim et al. (2011a), this study used the fifth-generation Pennsylvania State University/NCAR Mesoscale Model (MM5), together with the MM5 adjoint modeling system (Zou et al. 1997) and a Lanczos algorithm, to calculate TESVs. The model domain included  $70 \times 60$  horizontal grids (centered at  $36^\circ\text{N}$ ,  $125^\circ\text{E}$ ), with a 100-km horizontal resolution and 14 evenly spaced sigma levels in the vertical, from the surface to 50 hPa. The final analysis of the National Centers for Environmental Prediction (NCEP) (FNL;  $1^\circ \times 1^\circ$  global grid) was used for the initial and lateral boundary conditions of the model. Physical parameterizations used for the non-linear basic state integrations included the Grell

convective scheme, a bulk aerodynamic formulation of the planetary boundary layer, a simple radiation cooling scheme, horizontal and vertical diffusion, dry convective adjustment, and explicit treatment of cloud water, rain, snow, and ice. The same physical parameterizations were used in the TLM and adjoint model integrations, although the moist physics scheme used in the TLM and adjoint model integrations was large-scale precipitation instead of the Grell convective scheme and explicit treatment of cloud water, rain, snow, and ice, used in basic state integrations. These configurations of physics parameterizations are appropriate to show large-scale sensitivities due to the environmental effects as well as small-scale sensitivities close to the TC center, as indicated in Kim and Jung (2009b).

The TC best track of Regional Specialized Meteorological Center (RSMC) Tokyo-Typhoon center was used for analysis and bogusing. To simulate more realistic TCs, the bogusing method of Kwon and Cheong (2010) was applied to the forward forecasting of TC predictions with an idealized three-dimensional bogus vortex of an analytic empirical formula. The method showed hydrostatic imbalance in the middle layers inside the eyewall approximately 20–30 min after the initial time of model integration. Thus, the forward simulations of TCs started 6 h in advance of the initial time to obtain the hydrostatically balanced fields at the initial time. The TCs were simulated for 54 h including the spin-up time to reach the balanced state after typhoon bogusing, and then TESVs were calculated after 6 h of spin-up for the later 48 h.

## 3 Results

### 3.1 Cases

The TCs directly affecting the Korean Peninsula are defined as the TCs entering into the emergency area (northern region of  $28^\circ\text{N}$  and western region of  $132^\circ\text{E}$ ; National Typhoon Center 2011). The definition of indirect effect of TCs on the Korean Peninsula is based on several other criteria according to the National Typhoon Center (2011). The 25 TCs that affected the Korean Peninsula were among 230 TCs that were generated in the western North Pacific from 2001 to 2010 (National Typhoon Center 2011). A total of 21 TCs were chosen excluding some weak and large track forecasting error cases (Table 1) because both cause unrealistic sensitive regions. Since the TESV is calculated based on the TC forecast trajectory, the sensitive regions for the predicted basic state with large error may be quite different from that for the real (or analyzed) basic state, causing unrealistic sensitive regions. If the track forecast error was greater than 450 km at the final time

(48 h from the initial time), the case was treated as a large track forecast error case.

Based on the 3- or 6-hourly TC best position information from RSMC-Tokyo, the 48 h before approaching the Korean Peninsula was defined as the initial time of each case. The decision criterion of the final (verification) time was as follows: First, the time when a TC was nearest the Korean Peninsula including Jeju Island (the largest and southernmost island of Korea) was determined. If a TC passed over Jeju Island and then approached the Korean Peninsula, the final time was determined as the time a TC made its closest approach to Jeju Island. If a TC went through ET at the nearest time, the final time was determined as the time immediately before ET. If the nearest time happened to be some time after the TC passed over the Korean Peninsula, then the final time was determined as the time immediately before passing over the Korean Peninsula. The initial time was defined as the 48 h ahead of the final time.

The entire RSMC best tracks for the chosen TCs are shown in Fig. 1a and the 48-h tracks in Fig. 1b. Most of the

TCs generated within 5°–25°N and 120°–170°E passed through the region of 120°–140° E over 30°N and disappeared or transformed into extratropical cyclones within 130°–180°E over 40°N. During the simulated 48 h, most of the tracks started at the northern Philippine Sea and ended at the Yellow Sea, East China Sea, or East Sea/Japan Sea. Figure 2 shows the predicted TC tracks with the verification region in the model domain. On average, the predicted track error at the verification time was 182 km. To determine the predicted TC track (i.e., position of the TC center), the TC tracking method by Kim and Kim (2010) was used.

### 3.2 Clustering of the cases

Because the influence of TCs on the Korean Peninsula is determined mostly by TC tracks, statistical TESV distributions depending on TC tracks are evaluated. To determine the characteristics of TCs according to track, the clustering analysis based on a regression mixture model by

**Table 1** List of TCs affecting the Korean Peninsula during the past 10 years

No.	Name	TC number	Initial time	Class	Lat (N)	Lon (E)	Press (hPa)	Group
1	RAMMASUN	200205	2002070318	5	25.6	124.9	945	1
2	KALMAEGI	200807	2008071806	3	26.1	120.5	994	1
3	MALOU	201009	2010090412	3	27.0	127.0	998	1
4	LINFA	200304	2003052818	3	20.9	125.3	992	2
5	ETAU	200310	2003080612	5	23.9	128.8	955	2
6	MAEMI	200314	2003091006	5	24.0	126.6	910	2
7	MINDULLE	200407	2004070118	4	23.9	120.5	980	2
8	MEGI	200415	2004081618	3	21.2	128.8	992	2
9	SONGDA	200418	2004090418	5	25.1	129.7	925	2
10	EWINIAR	200603	2006070718	5	22.5	126.5	950	2
11	SHANSHAN	200613	2006091506	5	22.1	124.0	935	2
12	MAN-YI	200704	2007071200	5	21.0	129.2	930	2
13	NARI	200711	2007091400	5	24.4	129.4	960	2
14	PABUK	200111	2001081906	5	26.3	133.7	960	3
15	FENGSHEN	200209	2002072412	5	28.7	137.7	965	3
16	RUSA	200215	2002082900	5	27.6	131.3	950	3
17	NAMTHEUN	200410	2004073006	5	31.8	137.2	965	3
18	CHABA	200416	2004082806	5	27.4	133.6	935	3
19	NABI	200514	2005090400	5	24.8	132.2	940	3
20	WUKONG	200610	2006081718	3	32.0	131.1	980	3
21	USAGI	200705	2007073118	5	24.2	137.9	950	3
22	NAKRI	200208	2002071112	3	25.6	126.3	990	–
23	SOUDELOR	200306	2003061706	4	20.7	123.2	975	–
24	DIANMU	201004	2010080812	3	23.6	124.9	994	–
25	KOMPASU	201007	2010083012	4	23.7	131.2	980	–

The “Class” column represents the TC type [tropical storm (TS, 3), severe tropical storm (STS, 4), and Typhoon (TY, 5)], “Press” represents the central pressure of the TC by RSMC best track information, “Group” represents the clustered group number of each case. The 22nd to 25th TCs were excluded from the study

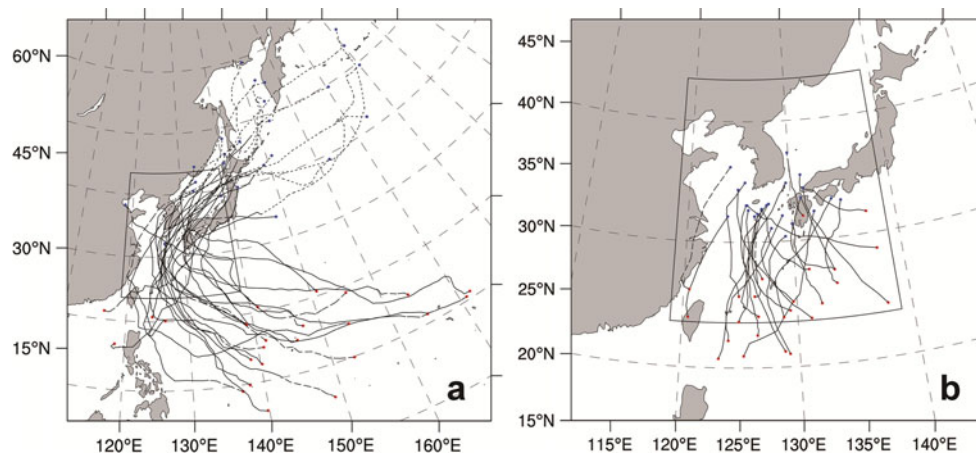


**Fig. 1** RSMC best tracks of the TCs that affected the Korean Peninsula from 2001 to 2010. **a** The entire tracks and **b** the tracks for the simulated 48 h. The solid lines are for tropical storm (TS), severe tropical storm (STS), and typhoon (TY), dashed lines are for the tropical depression (TD), and dotted lines are for the extratropical

cyclone. The red and blue dots in **a** are the generation and extinction positions of TCs, respectively. The red and blue dots in **b** are the initial and final positions of 48-h TC tracks. The box inside of the domain denotes the verification area

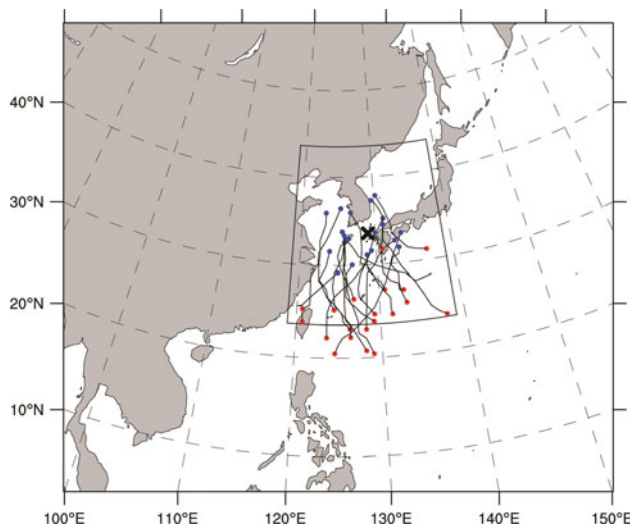


**Fig. 2** Model domain, the predicted TC tracks with the verification area (box), and the center of the region (X). The red and blue dots are the initial and final positions of 48-h predicted TC tracks

Camargo et al. (2007a) was applied. Previous studies (Hodanish and Gray 1993; Harr and Elsberry 1991, 1995a, b; Lander 1996; Elsner and Liu 2003; Elsner 2003; Hall and Jewson 2007; Camargo et al. 2007a, b, 2008; Nakamura et al. 2009; Kim et al. 2011b) noted that an effective way to explain characteristics of various TC tracks is to classify TC trajectories into a definite number of patterns. Recently, Camargo et al. (2007a) and Kim et al. (2011b) indicated that the optimal TC clustering number in the western North Pacific for the last several decades (approximately 40–50 years) is seven. In Camargo et al. (2007a), four of the seven groups passed the Korean Peninsula or the southern region of Japan. On the other hand,

Kim et al. (2011b) showed that three of the seven groups passed this same region. For the cases in the present study, the clustering group number was chosen to be three as in Kim et al. (2011b). The elements of clustering were the latitude and longitude of the forecasted TC tracks. Three groups are different in the 95 % significance level.

### 3.3 Characteristics of clustered groups

Figure 3 shows the clustered TC tracks for the simulated 48 h. The first group (group 1) includes three TCs that passed from the East China Sea to the Yellow Sea (Fig. 3a), the second group (group 2) includes ten TCs that passed from the northwestern Philippine Sea (east of Taiwan) to the southern sea of the Korean Peninsula (Fig. 3b), and the third group (group 3) includes eight TCs that passed from the northeastern Philippine Sea (south of Japan) to the East Sea (Fig. 3c).

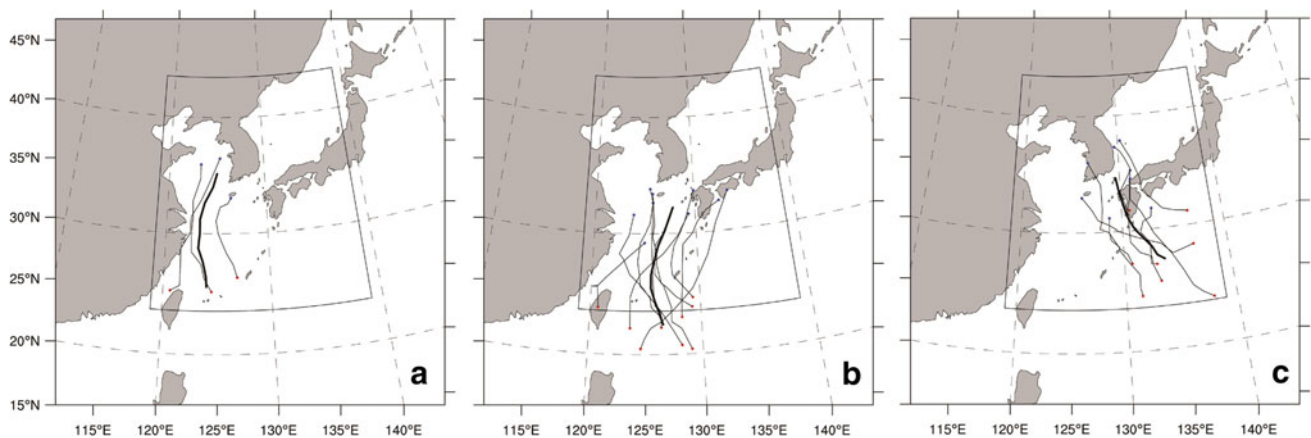
The relationships between the simulated TC positions and forecasting times of each group are given in Fig. 4. The average TC track of group 1 passed the most western region and was meridionally located between groups 2 and 3 before the 24-h forecast and moved to the most northern region after 24 h. Group 2 was zonally located between groups 1 and 3 and meridionally passed the most southern region. Group 3 passed the most eastern region for the entire forecast time and the northern region within 24 h. The northward moving speed of group 3 was the slowest compared to the other two groups. While groups 1 and 2 moved approximately 9.6° northward and 1.1° eastward for 48 h, group 3 moved approximately 7.1° northerly and 4.5° westerly for the same period. Groups 1 and 2 changed their direction from westward to eastward after 18 h.



To determine the relationship between average TC movement of each group and its environment, the mean sea level pressure (MSLP) and mean 500 hPa geopotential height with the average TC center of each group at 0, 24, and 48 h were compared and are shown in Fig. 5. In group 1, the subtropical ridge extended most closely to the TC center at the initial time compared to the other groups, then shrank and moved eastward and weakened during the next 48 h (Fig. 5a, d, and g). In other words, the ridge reached from the southern region of the Korean Peninsula to the Philippine Sea at the initial time, then shrank to the southeastern region of the Kyushu Island at the final time. Because of the weakening of the west edge of the subtropical ridge, the TC moved from the East China Sea to the Yellow Sea by changing the direction from westward to eastward after the 18-h forecast (not shown). As the mid-latitude trough moved eastward, the 5820-gpm line that merged with the TC center and the well-organized trough pattern in the midlatitude became weak after the 24-h forecast. On the sea level, the high-pressure region (1,008 hPa MSLP, shaded by orange and

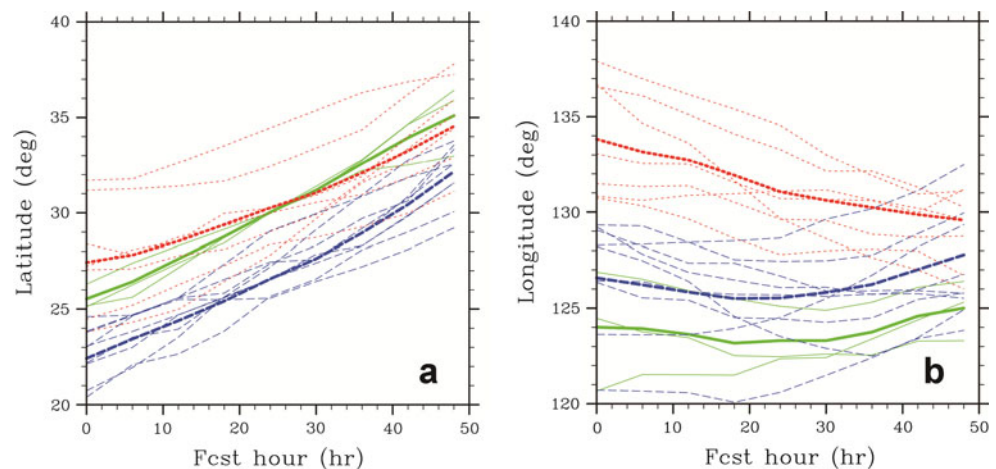
**Fig. 5** MSLP (shaded; interval of 2 hPa) and 500 hPa geopotential height (thin contour; interval of 30 gpm) superposed on the TC track (bold line and “X” marks for the initial and final time) with TC center position (black and big dot) and average steering flow of TC (white bold arrow) at 48 h for **a** group 1, **b** group 2, and **c** group 3, 24 h for **d** group 1, **e** group 2, and **f** group 3, and 00 h for **g** group 1, **h** group 2, and **i** group 3. The white bold arrow denotes the average steering flow of TC and the length represents the actual translation velocity with the dashed circle representing the scale of  $5 \text{ ms}^{-1}$ . The bold contour and dotted pattern denote the area over 5,880 gpm. The differences between 48 and 00 h MSLP (shaded; interval of 3 hPa), and the differences between 48 and 00 h 500 hPa geopotential height (contour; interval of 20 gpm; dotted for negative values) for **j** group 1, **k** group 2, and **l** group 3

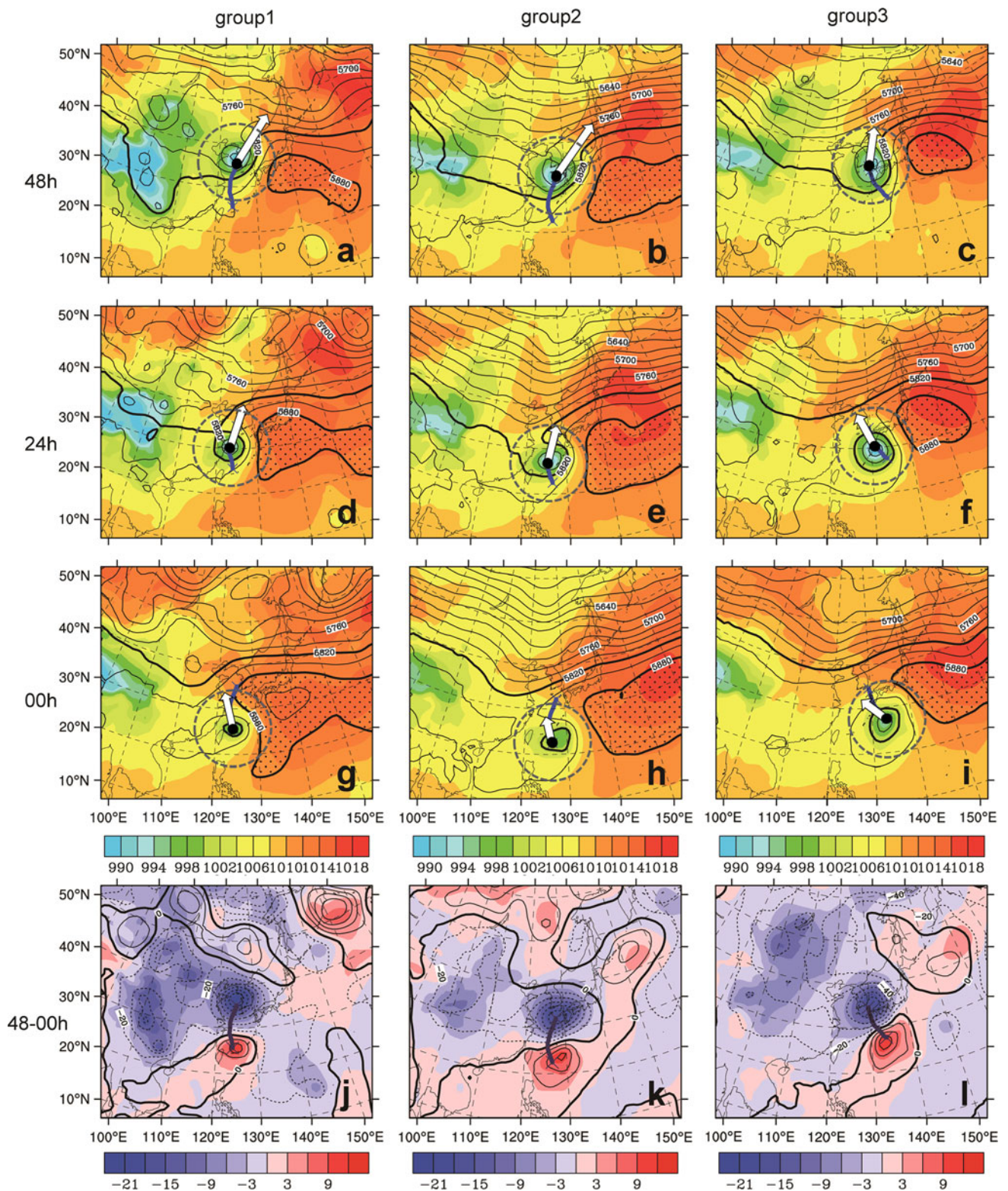
reddish color in Fig. 5) stretched from the Korean Peninsula to the northeastern part of China at the initial time. As time passed, the pressures fell as the subtropical ridge weakened and the mid-latitude trough and TC moved to that region (Fig. 5j). Initially northwestward-directed steering flow changed its direction to northeastward at the final time, and the steering speed increased as time passed (Fig. 5a, d, and g). The steering flow was defined as the deep layer mean flow from 1,000 to 100 hPa, with the



**Fig. 3** The predicted TC tracks for **a** group 1, **b** group 2, and **c** group 3. Bold lines are the averaged tracks of each group. The red and blue dots are the same as in Fig. 2

**Fig. 4** Relationship between the forecasting time and simulated TC positions of **a** latitude and **b** longitude. The solid green lines are for group 1, dashed blue lines are for group 2, and dotted red lines are for group 3, with the averages shown in bold lines





pressure-weighted wind function averaged over the 1–7° radially from the TC center (Neumann 1979; Naval Research Laboratory 1999).

In group 2, the subtropical ridge was located over the southern sea of Shikoku and Honshu Islands (Fig. 5b, e, and h). As time passed, the western boundary of the



subtropical ridge moved eastward. Compared to group 1, the location of the subtropical ridge did not change significantly. Similar to group 1, the TC recurved along the subtropical ridge, the mid-latitude trough moved eastward, and the 5,820-gpm line merged with the TC center after the 24-h forecast. The well-organized mid-latitude system at the initial time was well maintained during the 48-h forecast. Different from the group 1, the high-pressure pattern was shown over Manchuria during the entire forecast period even though it was weakened as the subtropical ridge shrank toward east (Fig. 5k). The steering flow of group 2 shows similar pattern to that of group 1, with more increasing speed. Because the magnitude of steering flow during 24–48 h ( $2.99 \text{ ms}^{-1}$ ) was larger than that during 00–24 h ( $1.76 \text{ ms}^{-1}$ ), the recurring of TCs was enhanced during the later 24 h (Fig. 5b, e, and h).

In group 3, the subtropical ridge moved to the northeastern region and shrank as time passed (Fig. 5c, f, and i). Different from groups 1 and 2, the subtropical ridge was located in the northern area of the TC center during the entire forecast period, and the mid-latitude trough moved very slowly toward the east (Fig. 5l). The axis of the trough reached from Manchuria to mid-eastern China. Initially northwestward-directed steering flow changed its direction to northward at the final time, and the steering speed did not increase much as time passed (Fig. 5c, f, and i). The locations of the subtropical ridge and mid-latitude trough and steering flow indicated that the TC steering was weak for TCs in this group. The 5,820-gpm line was merged with the TC at 42 h (not shown). Cyclone barely reaches latitude of ridge axis.

### 3.4 Characteristics of normalized average TESVs

#### 3.4.1 Horizontal structures

Figure 6 shows the normalized average TESV energy with 500 hPa geopotential height at the initial (Fig. 6a–d) and final times (Fig. 6e–h) of all 21 cases. Figure 6d and h is vertically integrated energy composites from the first to third TESVs according to (5). On average, the ratios of the second and third TESVs' singular values to the first TESV's singular value are 0.51 and 0.28, respectively. The sensitive regions appeared mainly near the mid-latitude trough and around the TC center. At the initial time, the largest TESV energy was near the mid-latitude trough and extended around the TC center. The maximum of the second TESV energy also resided in the mid-latitude trough, with the second largest TESV energy in the eastern region of the TC center. The composite TESV energy fields were similar to the energy fields of the first TESV because the weight of the first TESV was the largest according to (5). At the final time, the trough moved toward the east and located over the Korean Peninsula, and the sensitive regions resided around the trough and TC center in the verification region.

Because the normalized average energy of the composite TESV was similar to that of the first TESV, from now on, the first TESV was analyzed in more detail. Figure 7 shows the normalized average energy of the first TESV and average 500 hPa geopotential height of each group at the initial (Fig. 7a–c) and final times (Fig. 7d–f)

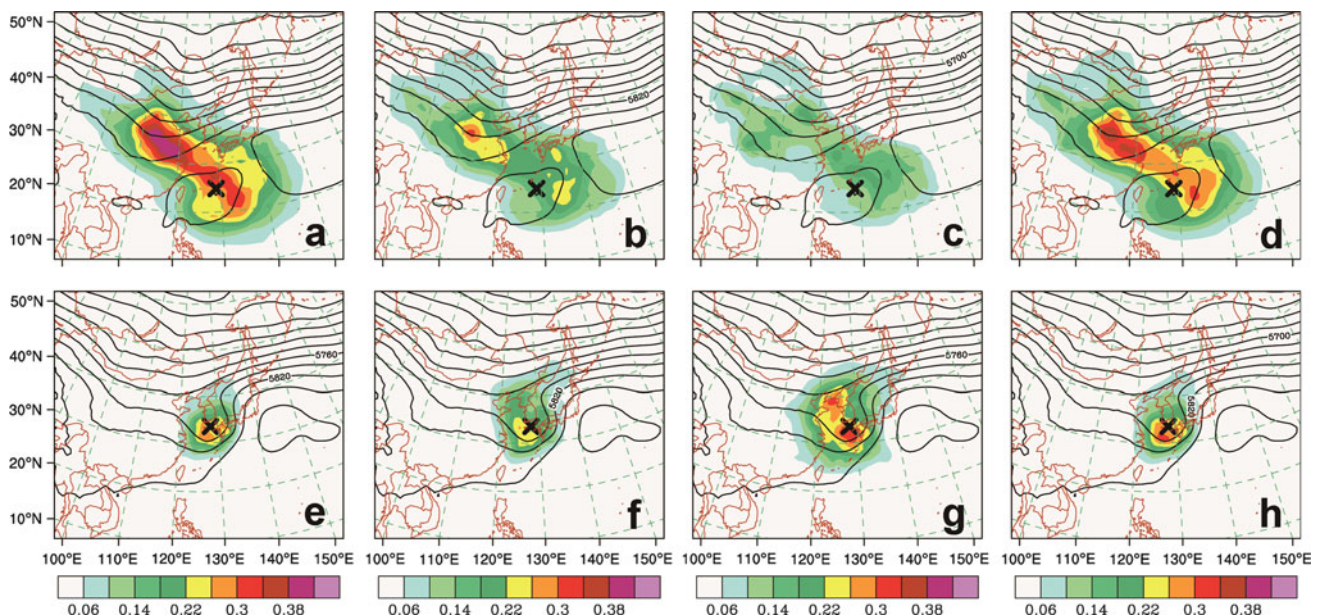


**Fig. 6** Normalized average, vertically integrated TE of TESVs (color shaded) and 500 hPa geopotential height (thin contour; interval of 30 gpm) with the center of the TC (X) at the initial (a–d) and final

times (e–h): **a, e** the first TESV; **b, f** the second TESV; **c, g** the third TESV; and **d, h** the composite TESV from the first to third



with the average TC tracks for 48 h. At the initial time, the TESV energy of all the groups was located around the TC centers and the troughs. In group 1, the maximum was on the trough, with the second largest value around the TC center (approximately 300–700 km from the TC center), similar to the previous studies (Kim and Jung 2009a; Peng and Reynolds 2006; Reynolds et al. 2009; and Wu et al. 2009b). In group 2, the patterns of TESV energy were similar to group 1, with a more prominent maximum on the trough than around the TC center. Compared to group 1, the TESV energy around the TC center was weak because the subtropical ridge was not extended toward west. In group 3, the TESV energy in the mid-latitude trough was weaker than in groups 1 and 2 but was stronger in the northeastern region of the TC center than in groups 1 and 2, as shown in Reynolds et al. (2009). The subtropical ridge existed in the northern part of the TESV energy maximum area in group 3.

To determine the sensitivity regions for each case of the cluster groups, the primary and secondary TE maxima of TESVs were calculated as shown in Fig. 8. As in Reynolds et al. (2009), the secondary maxima were defined as at least 50 % of the value of the primary

maxima and the secondary maxima regions were defined as spatially distinct (at least 500 km) locations from the primary maxima regions. If the location of the secondary maxima was not distinct from the primary maxima by the aforementioned criteria, then the regions with maxima between 25 and 50 % of the primary maxima were chosen as the secondary maxima regions. The primary maxima of group 1 existed in the eastern sea of Taiwan, the southern sea of Jeju Island, and inland China. The secondary maxima of group 1 were located in the eastern region of the Philippine Sea and inland China (Fig. 8a). The distributions of the primary and secondary TESV maxima in group 2 showed a more distinct separated pattern than in group 1 (Fig. 8b). The primary maxima were located in the middle-east China, a more northwestern region than the secondary maxima that were located in the south-eastern region and the Philippine Sea (Fig. 8b). Compared to groups 1 and 2, the locations of the primary and secondary maxima and TC centers were more eastward in group 3 (Fig. 8c). Most of the primary and secondary maxima of group 3 were located in the southern region of Japan, corresponding well with the high sensitivity regions shown in Fig. 7c, indicating that the normalized

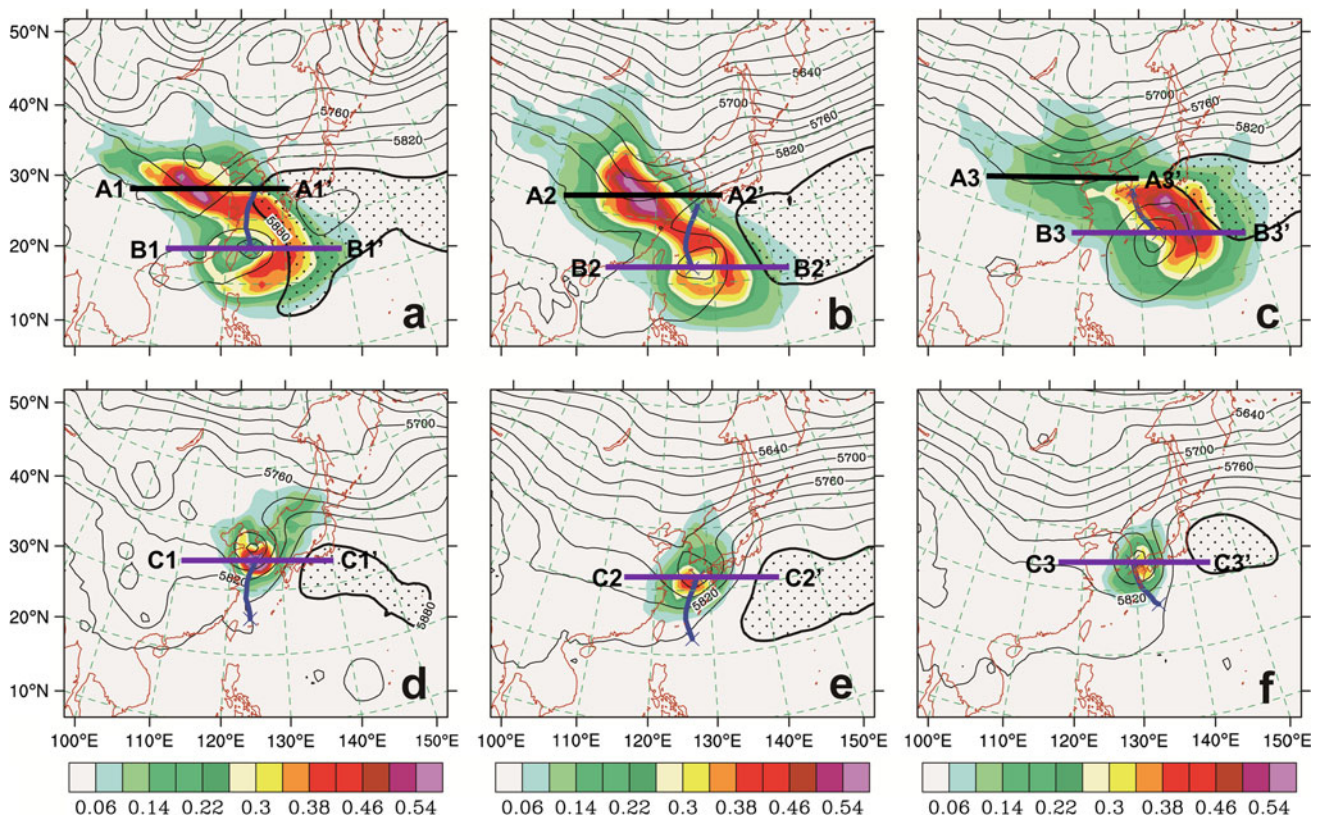


**Fig. 7** Normalized average, vertically integrated TE of the first TESVs (color shaded), 500 hPa geopotential height (thin contour; interval of 30 gpm), and average TC tracks (bold blue solid line) at the initial (a–c) and final times (d–f): **a, d** group 1; **b, e** group 2; and **c, f** group 3. The bold contour and shaded pattern denotes the area over 5,880 gpm. The lines are for vertical cross-sections (black for trough and purple for TC center)



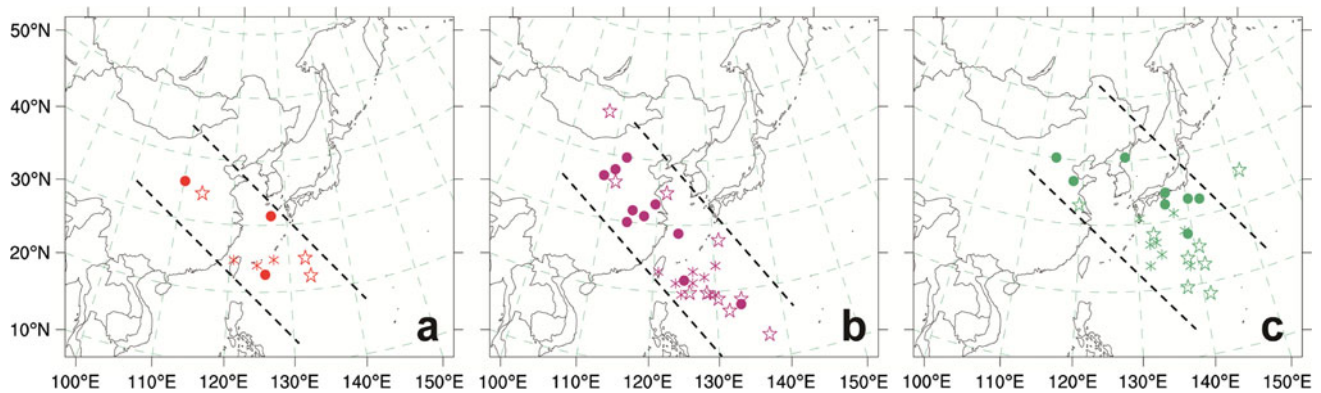


**Fig. 8** Locations of the center of TCs (asterisks), primary TE maxima (circles), and the secondary TE maxima (stars) of the first TESVs at the initial time for **a** group 1, **b** group 2, and **c** group 3. The dashed line indicates the rough guideline of the above positions

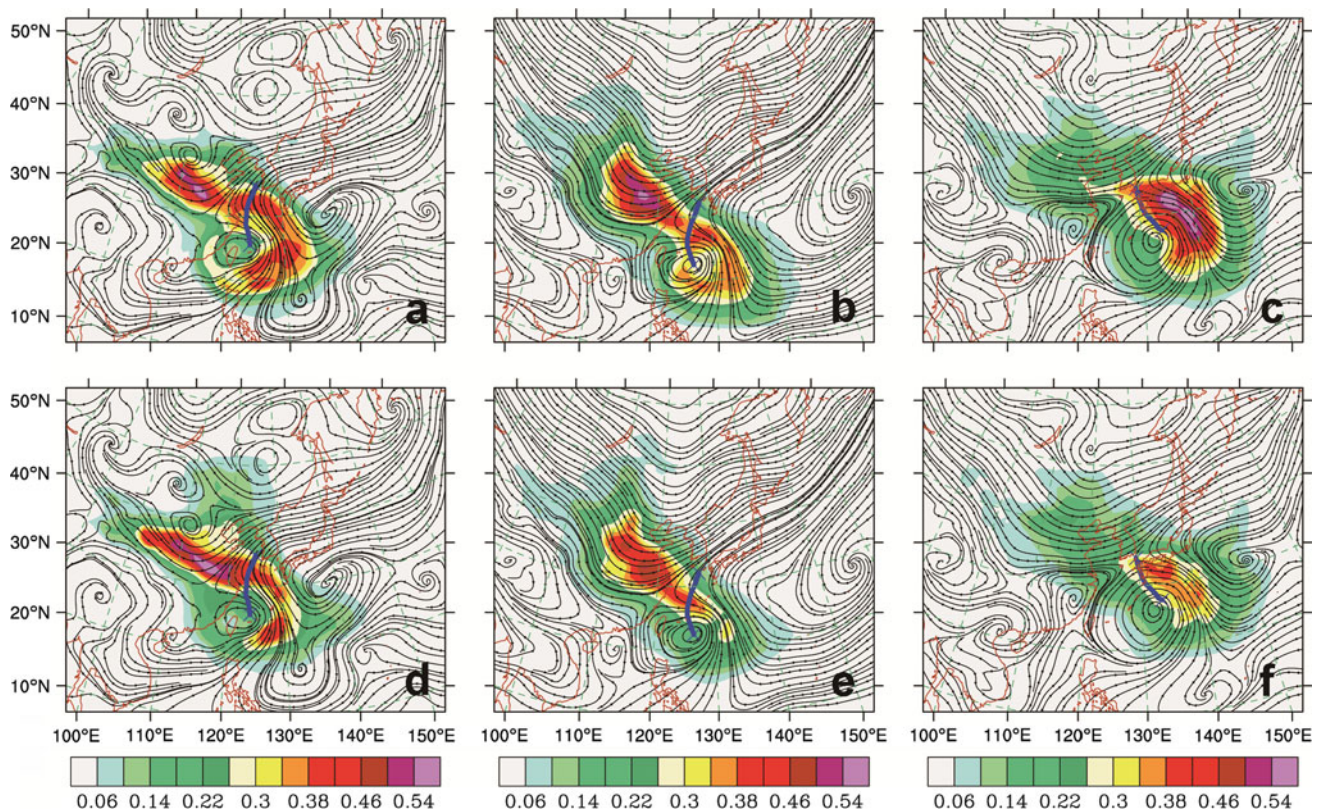


**Fig. 9** The 500 hPa streamlines (thin contour), and average TC tracks (bold blue solid line) at the initial time for normalized average, vertically integrated **a–c** KE of TESVs (color shaded) and **d–f** PE of TESVs (color shaded): **a, d** group 1, **b, e** group 2, and **c, f** group 3

average sensitivity distributions adequately represented the individual cases.

The TE of TESV can be divided into the kinetic energy (KE) and potential energy (PE) that reflect sensitivities to the wind and mass fields, respectively. According to Reynolds et al. (2009), the distribution of the KE and PE is related with the recurvature of the TC. Figure 9 shows the normalized average KE and PE of the first TESVs for each group. The KE had similar patterns with the TE in groups 1 and 2 (Fig. 9a, b), showing the sensitivity regions in the

mid-latitude trough and around the TC center. Maxima of KE were on the trough, which was different from Reynolds et al. (2009) that denoted the PE as dominant in the mid-latitude trough for the recurvature TC. This difference may be caused by the fact that the TCs in groups 1 and 2 include both recurvature and non-recurvature TCs. The major difference between KE and PE was in the southwestern region of the TC center where the PE was weaker than the KE. The KE of group 3 was much stronger than the PE, showing a similar pattern with its TE.



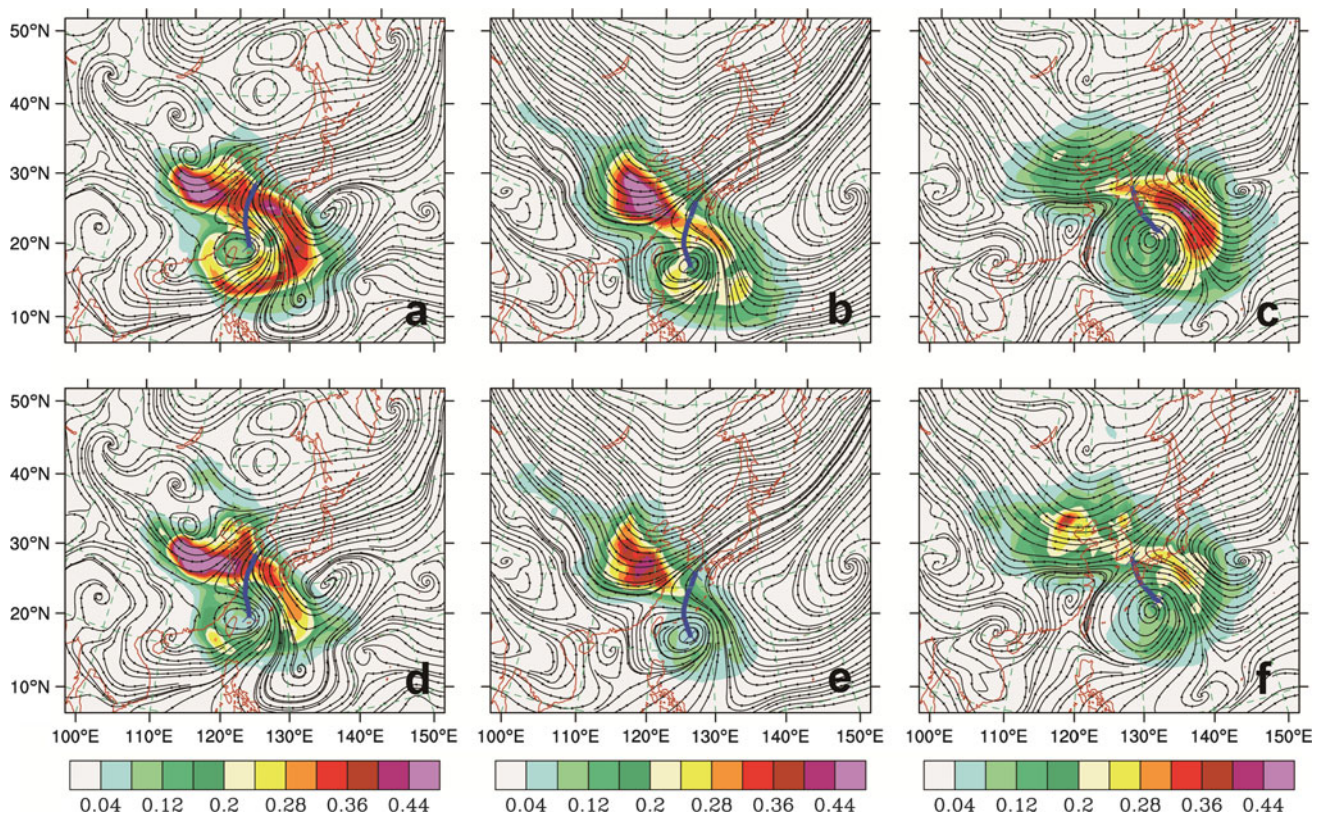


**Fig. 10** The same as in Fig. 9 except for the KE and PE in 500–800 hPa (color shaded)

To determine the KE and PE distributions in different vertical levels, the KE and PE were shown in three levels as in Kim et al. (2004b): 100–400 hPa (upper level), 500–800 hPa (middle level), and 850–1,000 hPa (lower level). In the middle level, the KE and PE patterns were similar with the patterns for the entire troposphere (Fig. 10), indicating that most of the KE and PE were distributed in the middle level.

### 3.4.2 Vertical structures

The vertical cross-sections of the normalized average TE of the first TESVs for each group are shown in Fig. 11. At the initial time, while groups 1 and 2 had baroclinic structures with westerly tilted potential vorticities (PVs) and TESVs in the trough (Fig. 11a, b), group 3 had sensitivity regions in the upper troposphere and showed much weaker baroclinicity in the trough (Fig. 11c). Around the TC centers, all groups showed generally symmetric patterns at the initial time (Fig. 11d–f). Different from the initial structures, the sensitivity maxima were located in the TC center at the final time (Fig. 11g–i). While the maximum PV of groups 2 and 3 appeared in the mid-upper troposphere, the maximum PV of group 1 was in the lower troposphere. The maximum TESVs of group 1 existed in the same region as the PV maximum, but there were two maxima in groups 2 and 3.

## 3.5 Characteristics of representative cases

### 3.5.1 Cases and horizontal TESV structures

Because the normalized average TE of TESVs could obscure the specific characteristics of each case, representative cases of each group were analyzed to elucidate the fine-scale structures (Figs. 12, 13, and 14). The representative cases of three groups were selected to have similar track patterns with their average in Fig. 3. The representative case of group 1 was TC KALMAEGI (0807) with the initial time of 06 UTC, 18 July 2008 (Fig. 12a). After the TC was formed in the northern sea of Taiwan, it moved northward along the east coast of China and arrived at the Yellow Sea at the final time. At the initial time, the subtropical ridge indicated by the 5,880-gpm line was located in the East China Sea and the western boundary of the Philippine Sea, and the trough was in the eastern region of China. The sensitive regions were located in the mid-latitude trough and around the TC center at the initial time. The maximum sensitivity existed in the southeastern region of the TC center, slightly different from the normalized average pattern of group 1 that had the maximum sensitivity in the mid-latitude trough and large sensitivity in the southeastern region of the TC center. The representative case of group 2 was TC NARI (0711) with the initial time



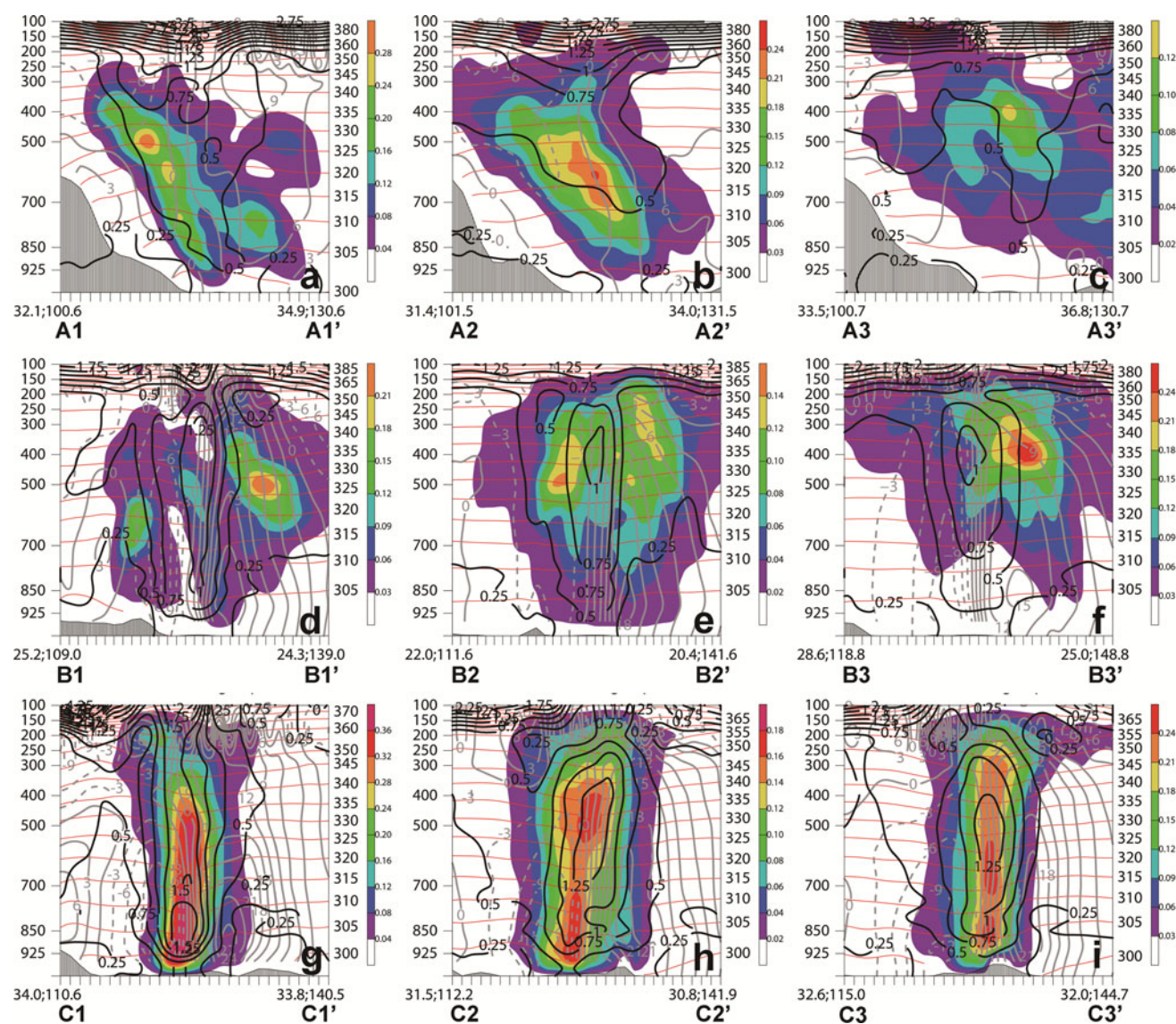


**Fig. 11** Vertical cross-sections along the west–east lines as indicated in Fig. 7 of the normalized average TE of the first TESVs (shaded contours) superposed on the PV (thick line; interval of 0.25 PVU),

potential temperature (red thin line; interval of 5 K), and meridional winds (gray thin line; interval of  $3 \text{ ms}^{-1}$ ): **a, d, g** group 1; **b, e, h** group 2; and **c, f, i** group 3. **a–f** 00 h and **g–i** 48 h

of 00 UTC, 14 September 2007 (Fig. 12b). The TC initiated in the eastern region of the Philippine Sea (east of Taiwan), moved westward, changed direction to northward after 24 h, and finally made landfall on Jeju Island. The subtropical ridge was located in the area extending from south of Japan to north of the Philippine Sea, and the trough was strong and well organized. The maximum sensitivity was in the mid-latitude trough, and the second largest sensitivity appeared in front of the TC but was not as distinct as TC KALMAEGI. The representative case of group 3 was TC USAGI (0705) (Fig. 12c). The TC initiated at the eastern boundary of the Philippine Sea at 18 UTC, 31 July 2007, moved northwestward, and arrived at Kyushu Island of Japan at the final time. Both the mid-

latitude trough and the subtropical ridge located in the east of the Philippine Sea were weak. The maximum sensitivities resided ahead of the TC, and the sensitivity in the mid-latitude trough was much weaker than those of groups 1 and 2.

### 3.5.2 Vertical TESV structures

The vertical cross-sections of the TE of the first TESVs in the zonal direction for each representative case are shown in Fig. 13. The PVs of KALMAEGI and NARI were the largest at the tropopause with upshear-tilted PV intrusions caused by upper tropopause folding under the mid-latitude trough at the initial time (Fig. 13a, b). The TESVs had also



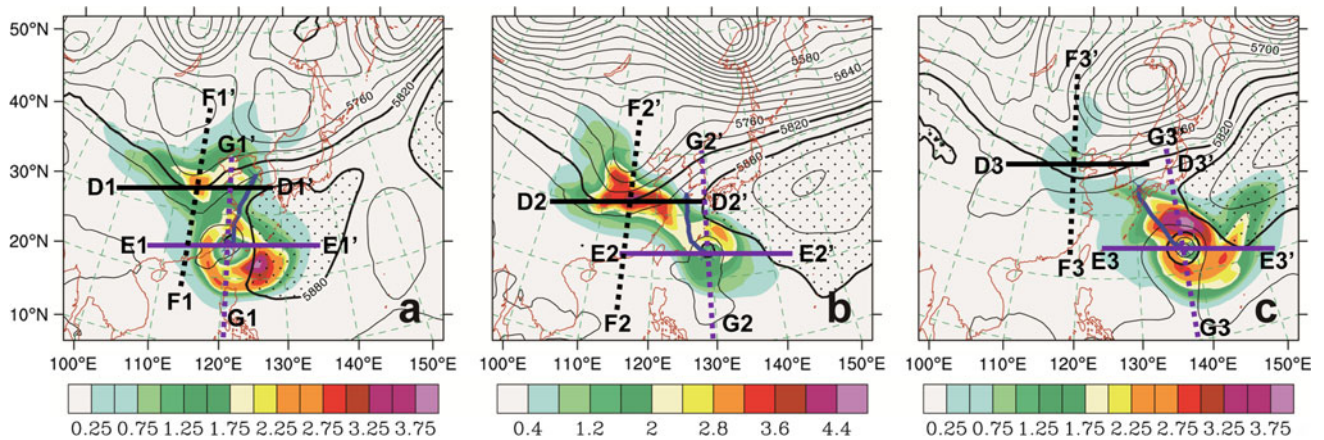


**Fig. 12** Vertically integrated TE of the first TESVs ( $10^{-3} \text{ J kg}^{-1}$ , color shaded), 500 hPa geopotential height (thin contour; interval of 30 gpm), and TC track (bold blue solid line) at the initial time for representative cases of each group: **a** KALMAEGI (06 UTC, 18 July 2008) of group 1, **b** NARI (00 UTC, 14 September 2007) of group 2,

and **c** USAGI (18 UTC, 31 July 2007) of group 3. The lines are for vertical cross-sections (black for trough and purple for TC center, bold lines for west-east cross-sections, and dotted lines for north-south cross-sections)

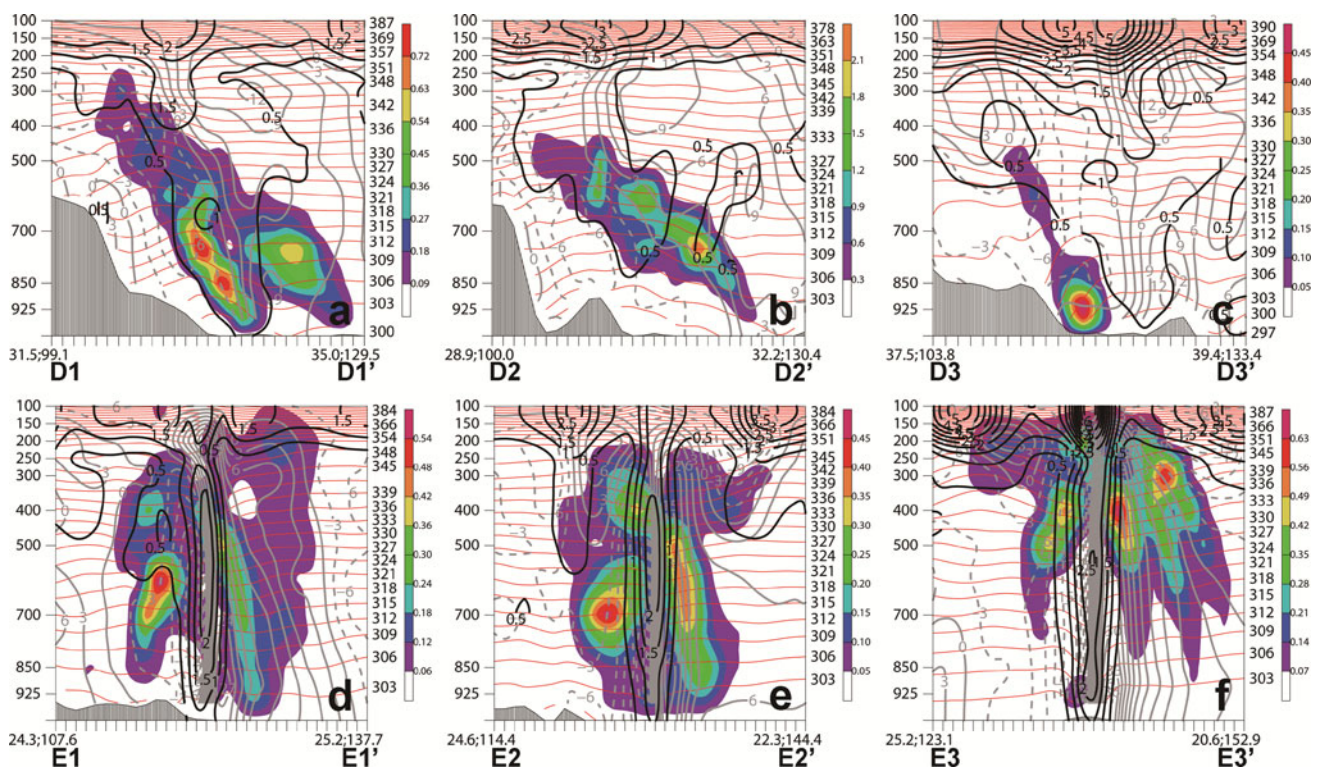


**Fig. 13** Vertical cross-sections along the west-east lines as indicated in Fig. 12 of TE of the first TESVs ( $10^{-3} \text{ J kg}^{-1}$ , shaded contours) superposed on PV (thick line; interval of 0.5 PVU), potential temperature (red thin line; interval of 3 K), and meridional winds

(gray thin lines; interval of  $3 \text{ ms}^{-1}$ ) for **a, d** KALMAEGI; **b, e** NARI; and **c, f** USAGI: **a–c** around mid-latitude trough and **d–f** near TC center

upshear-tilted structures similar to PV, and the large TESVs were distributed at the lower-to-mid-troposphere under the large PV. The meridional winds had westerly tilted structures, and their directions changed distinctively along the axis of the intruded PV maxima, showing that they were northerly in the western region of the axis and

southerly in the eastern region. These wind fields showed much clearer patterns than those in the averaged field in Fig. 11. Accordingly, the baroclinicities existed near the troughs of KALMAEGI and NARI. The vertical cross-sections of USAGI were different from KALMAEGI and NARI (Fig. 13c). There was also PV intrusion, but the



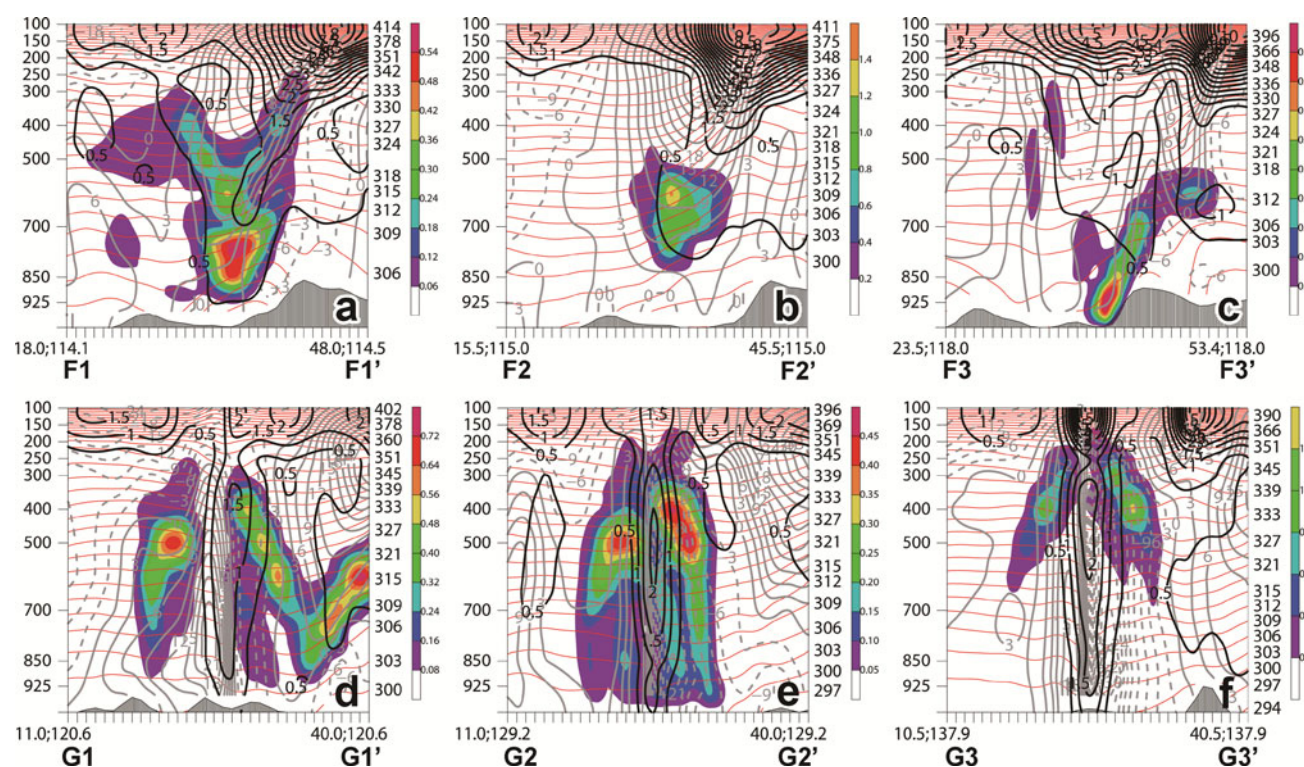


**Fig. 14** Vertical cross-sections along the north–south lines as indicated in Fig. 12 of TE of the first TESVs ( $10^{-3} \text{ J kg}^{-1}$ , shaded contours) superposed on PV (thick line; interval of 0.5 PVU), potential temperature (red thin line; interval of 3 K), and zonal

winds (gray thin lines; interval of  $3 \text{ ms}^{-1}$ ) for **a, d** KALMAEGI; **b, e** NARI; and **c, f** USAGI: **a–c** around mid-latitude trough and **d–f** near TC center

upshear-tilted structure was weaker than that of KALMAEGI and NARI. The largest TESV energy was not very tilted and was located in the western region of 0.5 PVU in the lower troposphere. The meridional wind was also not tilted.

Around the TC center for all three cases, the PVs, TESVs, and meridional winds had nearly symmetric structures (Fig. 13d–f). The PVs were the largest at the TC center and were not tilted. The TESV maxima of KALMAEGI and NARI were at the mid-troposphere, showing asymmetry in detailed structures: maxima of TESVs at the western region of the TC center were larger than at the eastern region of the TC center and had oval shapes tilted to the TC center, different from those in the eastern region (Fig. 13d, e). For USAGI, the maximum region appeared at the upper troposphere, different from groups 1 and 2 (Fig. 13f).

The vertical cross-sections of TE of the first TESVs in the meridional direction for each representative case are shown in Fig. 14. For KALMAEGI and NARI, the large poleward-tilted PVs at the tropopause intruded to the surface at high latitude, and the maximum TESVs were located under the intruded PVs (0.5 PVU) and the upper-level jet, similar to Reynolds et al. (2001) (Fig. 14a, b). The jet stream was located in the lower latitude, compared

to maximum PVs of the tropopause. There were large westerly wind gradients around the PV folding (over 1.0 PVU). For USAGI, the TESVs were tilted poleward, different from groups 1 and 2 (Fig. 14c). Around the TCs, the vertical cross-sections were roughly similar for the three cases (Fig. 14d–f). The cyclonic circulations occurred around the TC centers and the westerlies caused by mid-latitude troughs were observed around  $7^{\circ}\text{N}$  from the TC center.

#### 4 Summary and discussion

In the present study, TESVs for TC forecasts were calculated and evaluated during the past 10 years to investigate the statistical sensitivity distributions of TC forecasts affecting the Korean Peninsula. Therefore, the verification region was defined to include the Korean Peninsula. To simulate TCs more realistically to obtain more accurate sensitive regions, a typhoon bogusing was applied to the forward forecasting 6 h before the initial time to obtain hydrostatically balanced fields at the initial time.

A total of 21 TCs that affected the Korean Peninsula during the past 10 years were classified into three groups by clustering the TC tracks. The statistically sensitive



regions of the TCs were mainly in the mid-latitude trough and around the TC centers at the initial time. The three groups had characteristic environmental conditions such as subtropical highs and mid-latitude troughs. The first group passed from the East China Sea to the Yellow Sea, the second group passed from the northwestern Philippine Sea (east of Taiwan) to the southern sea of the Korean Peninsula, and the third group passed from the northeastern Philippine Sea (south of Japan) to the East Sea/Japan Sea. Nearly half of the TCs (ten of 21 TCs) were included in the second group.

The relationship between TC movement and its environment was analyzed. Holland and Wang (1995) demonstrated that the TC recurvature occurs through an unbroken subtropical high at the initial time and is substantially enhanced by a mid-latitude trough. Corresponding to Holland and Wang (1995), the TCs in groups 1 and 2 moved along the boundary and changed direction by the subtropical ridges. As the TCs moved northward and the mid-latitude troughs moved eastward, the recurvature was enhanced. The TCs had the maximum sensitive regions located in the mid-latitude troughs and largely sensitive regions around the TC center. However, depending on the extension of subtropical ridge, the primary sensitive regions were changed. Therefore, the group 2 has relatively weak sensitive regions around the TC center compared to group 1. Conversely, the TC steering was weak for TCs in group 3, where the sensitive regions were located around the TC center.

To understand the dynamic features associated with TESV sensitivities near the TC centers and in the mid-latitude troughs, the vertical structures were examined. While the first and second groups had westerly tilted TESV and PV structures associated with baroclinic environments in the mid-latitude trough at the initial time, the third group showed weak baroclinicity. In groups 1 and 2, the large poleward-tilted PVs at the tropopause in the high latitude intruded to the surface, and the maxima TESVs were located under the intruded PVs (0.5 PVU) and the upper-level jet, in agreement with Reynolds et al. (2001). The symmetric patterns were distinct for all groups around the TC centers at the final time, and the TESV maxima were located at the center of the TC at the final time.

Even though some specific characteristics of individual cases were different with those of the average fields, the analysis of the representative TC cases showed that the average pattern of the sensitivity regions and atmospheric systems roughly demonstrated characteristics of individual cases. Given the results in the present study, TCs moving toward a fixed verification region over the Korean Peninsula have different sensitivity regions and structures according to their moving tracks and the characteristic environmental conditions. For group 1 TCs, adaptive

observations both in mid-latitude trough and around TC center would be beneficial for TC forecasts affecting the Korean Peninsula. While the adaptive observations near the mid-latitude trough would be beneficial for group 2 TCs, those around the TC center would be beneficial for group 3 TCs. Because the mid-latitude troughs approaching the Korean Peninsula are mostly located in upstream regions in mainland China, it is difficult to do adaptive observations over those regions. Making use of satellite data efficiently over those upstream regions would be beneficial for adaptively observing TCs affecting the Korean Peninsula.

**Acknowledgments** The authors thank two anonymous reviewers for their valuable comments. The authors thank Dr. In-Hyuk Kwon and Prof. Hyung-Bin Cheong for providing the bogusing method for the typhoon simulation. This study was supported by the Korea Meteorological Administration Research and Development Program under grant CATER 2012-2030.

**Open Access** This article is distributed under the terms of the Creative Commons Attribution License which permits any use, distribution, and reproduction in any medium, provided the original author(s) and the source are credited.

## References

- Buizza R (1994) Localization of optimal perturbations using a projection operator. *Q J R Meteor Soc* 120:1647–1681
- Buizza R, Montani A (1999) Targeting observations using singular vectors. *J Atmos Sci* 56:2965–2985
- Byun K-Y, Lee T-Y (2012) Remote effects of tropical cyclones on heavy rainfall over the Korean peninsula statistical and composite analysis. *Tellus A* 64:14983. doi:[10.3402/tellusa.v64i0.14983](https://doi.org/10.3402/tellusa.v64i0.14983)
- Camargo SJ, Robertson AW, Gaffney SJ, Smyth P, Ghil M (2007a) Cluster analysis of typhoon tracks. Part I: general properties. *J Clim* 20:3635–3653
- Camargo SJ, Robertson AW, Gaffney SJ, Smyth P, Ghil M (2007b) Cluster analysis of typhoon tracks. Part II: large-scale circulation and ENSO. *J Clim* 20:3654–3676
- Camargo SJ, Robertson AW, Barnston AG, Ghil M (2008) Clustering of eastern North Pacific tropical cyclone tracks: ENSO and MJO effects. *Geochim Geophys Geosyst* 9:Q06V05. doi:[10.1029/2007GC001861](https://doi.org/10.1029/2007GC001861)
- Chen J-H, Peng MS, Reynolds CA, Wu C-C (2009) Interpretation of tropical cyclone forecast sensitivity from the singular vector perspective. *J Atmos Sci* 66:3383–3400
- Dorst NM (2007) The National Hurricane Research Project: 50 years of research, rough rides, and name changes. *Bull Am Meteor Soc* 88:1566–1588
- Ehrendorfer M, Errico RM (1995) Mesoscale predictability and the spectrum of optimal perturbations. *J Atmos Sci* 52:3475–3500
- Elsner JB (2003) Tracking hurricanes. *Bull Am Meteor Soc* 84:353–356
- Elsner JB, Liu KB (2003) Examining the ENSO–typhoon hypothesis. *Clim Res* 25:43–54
- Frank WM (1977a) The structure and energetics of the tropical cyclone I: storm structure. *Mon Weather Rev* 105:1119–1135
- Frank WM (1977b) The structure and energetics of the tropical cyclone II: dynamics and energetics. *Mon Weather Rev* 105:1136–1150

- Gelaro R, Langland RH, Rohaly GD, Rosmond TE (1999) An assessment of the singular-vector approach to targeted observing using the FASTEX dataset. *Q J R Meteor Soc* 125:3299–3327
- Hall TM, Jewson S (2007) Statistical modelling of North Atlantic tropical cyclone tracks. *Tellus* 59A:486–498
- Harr PA, Elsberry RL (1991) Tropical cyclone track characteristics as a function of large-scale circulation anomalies. *Mon Weather Rev* 119:1448–1468
- Harr PA, Elsberry RL (1995a) Large-scale circulation variability over the tropical western North Pacific. Part I: spatial patterns and tropical cyclone characteristics. *Mon Weather Rev* 123:1225–1246
- Harr PA, Elsberry RL (1995b) Large-scale circulation variability over the tropical western North Pacific. Part II: persistence and transition characteristics. *Mon Weather Rev* 123:1247–1268
- Ho C-H, Baik J-J, Kim J-H, Gong D-Y, Sui C-H (2004) Interdecadal changes in summertime typhoon tracks. *J Clim* 17:1767–1776
- Hodanish S, Gray WM (1993) An observational analysis of tropical cyclone recurvature. *Mon Weather Rev* 121:2665–2689
- Holland GJ, Wang Y (1995) Baroclinic dynamics of simulated tropical cyclone recurvature. *J Atmos Sci* 52:410–426
- Jung B-J, Kim HM, Zhang F, Wu C-C (2012) Effect of targeted dropsonde observations and best track data on the track forecasts of Typhoon Sinlaku (2008) using an Ensemble Kalman Filter. *Tellus A* 64:14984. doi:10.3402/tellusa.v64i0.14984
- Kim HM, Jung B-J (2006) Adjoint-based forecast sensitivities of Typhoon Rusa. *Geophys Res Lett* 33:L21813. doi:10.1029/2006GL027289
- Kim HM, Jung B-J (2009a) Singular vector structure and evolution of a recurving tropical cyclone. *Mon Weather Rev* 137:505–524
- Kim HM, Jung B-J (2009b) Influence of moist physics and norms on singular vectors for a tropical cyclone. *Mon Weather Rev* 137:525–543
- Kim J, Kim HM (2010) Development of a tropical cyclone tracker and application to tropical cyclones occurred in 2008 in North western Pacific. Abstract A41B-0070 presented at 2010 Fall Meeting, AGU, San Francisco, California, 13–17 Dec
- Kim HM, Morgan MC (2002) Dependence of singular vector structure and evolution on the choice of norm. *J Atmos Sci* 59:3099–3116
- Kim HM, Morgan MC, Morss RE (2004a) Evolution of analysis error and adjoint-based sensitivities: implications for adaptive observations. *J Atmos Sci* 61:795–812
- Kim HM, Youn Y-H, Chung H-S (2004b) Potential vorticity thinking as an aid to understanding midlatitude weather systems. *J Korean Meteor Soc* 40:633–647
- Kim HM, Kim S-M, Jung B-J (2011a) Real-time adaptive observation guidance using singular vectors for Typhoon Jangmi (200815) in T-PARC 2008. *Weather Forecast* 26:634–649
- Kim H-S, Kim J-H, Ho C-H, Chu P-S (2011b) Pattern classification of typhoon tracks using the fuzzy c-means clustering method. *J Clim* 24:488–508
- Kurihara Y, Tuleya RE (1974) Structure of a tropical cyclone developed in a three-dimensional numerical simulation model. *J Atmos Sci* 31:893–919
- Kwon I-H, Cheong H-B (2010) Tropical cyclone initialization with a spherical high-order filter and an idealized three-dimensional bogus vortex. *Mon Weather Rev* 138:1344–1367
- Kwon YC, Frank WM (2005) Dynamic instabilities of simulated hurricane-like vortices and their impacts on the core structure of hurricanes. Part I: dry experiments. *J Atmos Sci* 62:3955–3973
- Kwon YC, Frank WM (2008) Dynamic instabilities of simulated hurricane-like vortices and their impacts on the core structure of hurricanes. Part II: moist experiments. *J Atmos Sci* 65:106–122
- Lander MA (1996) Specific tropical cyclone track types and unusual tropical cyclone motions associated with a reverse-oriented monsoon trough in the western North Pacific. *Weather Forecast* 11:170–186
- Lang STK, Jones SC, Leutbecher M, Peng MS, Reynolds CA (2012) Sensitivity, structure, and dynamics of singular vectors associated with Hurricane Helene (2006). *J Atmos Sci* 69:675–694
- Majumdar SJ, Aberson SD, Bishop CH, Buizza R, Peng MS, Reynolds CA (2006) A comparison of adaptive observing guidance for Atlantic tropical cyclones. *Mon Weather Rev* 134:2354–2372
- Montani A, Thorpe AJ, Buizza R, Unden P (1999) Forecast skill of the ECMWF model using targeted observations during FASTEX. *Q J R Meteor Soc* 125:3219–3240
- Nakamura J, Lall U, Kushnir Y, Camargo SJ (2009) Classifying North Atlantic tropical cyclone tracks by mass moments. *J Clim* 22:5481–5494
- National Typhoon Center (2011) Typhoon white book. Korean Meteorological Administration, Korea, pp 224–225
- Naval Research Laboratory (1999) Tropical cyclone forecasters' reference guide. Chapter 4-1. Influences on tropical cyclone motion. <http://www.nrlmry.navy.mil/~chu/chap4/se100.htm>. Accessed 14 July 2012
- Neumann CJ (1979) On the use of deep-layer-mean geopotential height fields in statistical prediction of tropical cyclone motion. In: 6th conference on probability and statistics in atmospheric sciences. American Meteorological Society, Boston, pp 32–38
- Palmer TN, Gelaro R, Barkmeijer J, Buizza R (1998) Singular vectors, metrics, and adaptive observations. *J Atmos Sci* 55:633–653
- Peng MS, Reynolds CA (2005) Double trouble for typhoon forecasters. *Geophys Res Lett* 32:L02810. doi:10.1029/2004GL021680
- Peng MS, Reynolds CA (2006) Sensitivity of tropical cyclone forecasts as revealed by singular vectors. *J Atmos Sci* 63:2508–2528
- Rappaport EN et al (2009) Advances and challenges at the National Hurricane Center. *Weather Forecast* 24:395–419
- Reynolds CA, Gelaro R, Rosmond R (2001) Relationship between singular vectors and transient features in the background flow. *Q J R Meteor Soc* 127:1731–1760
- Reynolds CA, Peng MS, Chen J-H (2009) Recurring tropical cyclones: singular vector sensitivity and downstream impact. *Mon Weather Rev* 137:1320–1337
- Wang Y (2002) Vortex Rossby Waves in a numerically simulated tropical cyclone. Part II: the role in tropical cyclone structure and intensity changes. *J Atmos Sci* 59:1239–1262
- Wang Y, Holland GJ, Leslies LM (1993) Some baroclinic aspects of tropical cyclone motion. In: Lighthill J, Emmanuel K, Holland G (eds) Tropical cyclone disaster. Beijing University Press, China, pp 280–285
- Wu CC, Chen J-H, Lin P-H, Chou K-H (2007) Targeted observations of tropical cyclone movement based on the adjoint-derived sensitivity steering vector. *J Atmos Sci* 64:2611–2626
- Wu CC, Chen S-G, Chen J-H, Chou K-H, Lin P-H (2009a) Interaction of Typhoon Shanshan (2006) with the midlatitude trough from both adjoint-derived sensitivity steering vector and potential vorticity perspectives. *Mon Weather Rev* 137:852–862
- Wu CC, Chen J-H, Majumdar SJ, Peng MS, Reynolds CA, Aberson SD, Buizza R, Yamaguchi M, Chen S-G, Nakazawa T, Chou K-H (2009b) Intercomparison of targeted observation guidance for tropical cyclones in the Northwestern Pacific. *Mon Weather Rev* 137:2471–2492
- Zou X, Vandenberghe F, Pondeva M, Kuo Y-H (1997) Introduction to adjoint techniques and the MM5 adjoint modeling system. NCAR Technical Note NCAR/TN- 435STR, pp 110